Solvent and pH Dependent Fluorescent Properties of a Dimethylaminostyryl Borondipyrromethene Dye in Solution

Mukulesh Baruah,[†] Wenwu Qin,[†] Cristina Flors,[†] Johan Hofkens,[†] Renaud A. L. Vallée,[†] David Beljonne,[‡] Mark Van der Auweraer,[†] Wim M. De Borggraeve,[†] and Noël Boens*[,†]

Department of Chemistry, Katholieke Universiteit Leuven, Celestijnenlaan 200F, 3001 Leuven, Belgium, and Laboratory for Chemistry of Novel Materials, University of Mons-Hainaut, Place du Parc 20, 7000 Mons, Belgium

Received: August 29, 2005; In Final Form: January 23, 2006

Steady-state and time-resolved fluorescence techniques have been used to study the photophysical properties of the fluorescent BODIPY-derived dye 3-{2-[4-(dimethylamino)phenyl]ethenyl}-4,4-difluoro-8-(4-methoxyphenyl)-1,5,7-trimethyl-3a,4a-diaza-4-bora-*s*-indacene. This compound has been synthesized via a microwave-assisted condensation of *p*-*N*,*N*-dimethylaminobenzaldehyde with the appropriate 1,3,5,7-tetramethyl substituted borondipyrromethene unit. The fluorescence properties of the dye are strongly solvent dependent: increasing the solvent polarity leads to lower fluorescence quantum yields and lifetimes, and the wavelength of maximum fluorescence emission shifts to the red. The Catalán solvent scales are found to be the most suitable for describing the solvatochromic shifts of the fluorescence emission. These are dominated by polarity/polarizability effects, as confirmed by quantum-chemical calculations performed in the dielectric continuum approximation. Fluorescence decay profiles of the dye can be described by a single-exponential fit in most solvents investigated, while two decay times are found in alcohols. The dye undergoes a reversible protonation−deprotonation reaction in the acidic pH range with a pK_a of 2.25 in acetonitrile solution. Fluorimetric titrations as a function of pH produce fluorescence emission enhancements at lower pH. The fluorescence excitation spectra show a hypsochromic shift from 600 nm for the neutral amine to 553 nm for the ammonium form, so that ratiometric measurements can be used to determine pK_a.

1. Introduction

The design and synthesis of novel, fluorescent chemosensors for the measurement of analytically important ions and molecules continues to be an exciting area of research.[1,2] In recent years, much attention has been focused on the synthesis of 4,4-difluoro-4-bora-3a,4a-diaza-*s*-indacene[3] (borondipyrromethene or BODIPY) based fluorescent probes and their application as selective and efficient chemosensors.[4] The abundant applications of borondipyrromethene derivatives are facilitated by the commercial availability of a range of BODIPY dyes,[2] and they are illustrated by a selection of recent papers describing BODIPY analogues as fluorescent probes for H^+,[5] Na^+,[6] K^+,[7] Ca^{2+},[8] Ag^+,[9] and Zn^{2+},[10] as photocleavable fluorescent nucleotides in four-color DNA sequencing,[11] and as activity-based fluorescent probes for protein and kinases.[12] BODIPY is a well-known fluorophore characterized by valuable properties such as high (photo)chemical stability and relatively high fluorescence quantum yields (often approaching 1.0) and absorption coefficients.[5,13−23] Moreover, borondipyrromethene dyes are excitable with visible light, have narrow emission bandwidths with high peak intensities, and are amenable to structural modification.

In this work, we synthesized—via a microwave-assisted condensation reaction—a fluorescent pH sensor with 3a,4a-diaza-4-bora-*s*-indacene as fluorophore linked to a *p*-*N*,*N*-dimethylaminostyryl group at the 3-position. To investigate the photophysical properties of this new BODIPY dye (**1**), we recorded its steady-state absorption and fluorescence excitation and emission spectra and collected its time-resolved fluorescence profiles in several solvents. From these experiments, we determined the position of the spectral maxima (λ_{abs}, λ_{ex}, and λ_{em}), the full width at half-maximum of the absorption band (fwhm$_{abs}$), the Stokes shifts ($\Delta\bar{\nu} = \bar{\nu}_{abs} - \bar{\nu}_{em}$), the fluorescence quantum yields (ϕ_f) and lifetimes (τ), and the rate constants of radiative (k_f) and nonradiative (k_{nr}) deactivation of this compound. We used the Lippert solvent parameter Δf, the normalized $E_T^N(30)$ polarity scale, and the multiparameter Kamlet−Taft and Catalán solvent scales to describe the solvent effect on the fluorescence emission maxima and Stokes shift of **1**. Semiempirical quantum-chemical calculations were performed to assess the amount of charge transfer in the excited state and explore the solvent dependent absorption and emission properties of the dye. Finally, fluorimetric titrations as a function of pH were used to determine the pK_a of the new dye in acetonitrile.

2. Results and Discussion

2.1. Synthesis. 4,4-Difluoro-8-(4-methoxyphenyl)-1,3,5,7-tetramethyl-3a,4a-diaza-4-bora-*s*-indacene (**4**) was synthesized from *p*-methoxybenzaldehyde (**2**) and 2,4-dimethylpyrrole (**3**) following a literature procedure.[24] Compound **1** was synthesized in 26% yield by microwave-assisted condensation of compound **4** with *p*-*N*,*N*-dimethylaminobenzaldehyde (**5**) using acetic acid−piperidine as a catalyst (Scheme 1). The use of microwave irradiation drastically reduced the reaction time (from 26 h for conventional heating to 15 min for microwave heating) without affecting the chemical yield.

* To whom correspondence should be addressed. E-mail: Noel.Boens@chem.kuleuven.be.
[†] Katholieke Universiteit Leuven.
[‡] University of Mons-Hainaut.

10.1021/jp054878u CCC: $33.50
Published on Web 04/20/2006

SCHEME 1: Synthesis of Compound 1

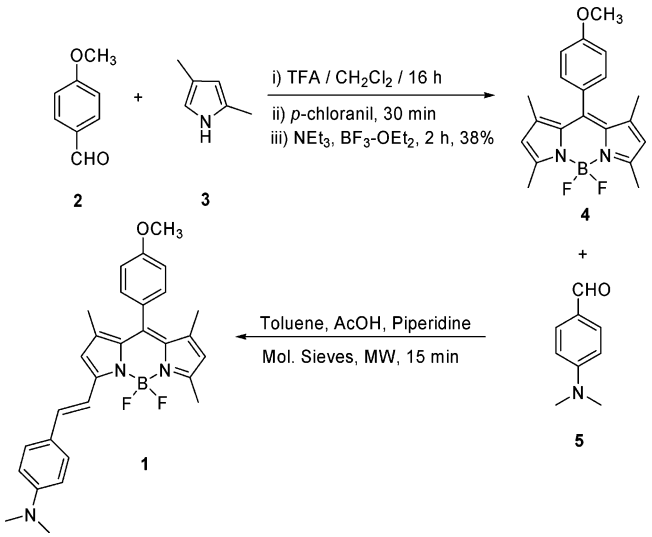

2.2. Spectroscopic Properties. The UV/vis absorption and fluorescence emission spectra of **1** dissolved in several solvents are depicted in Figure 1. The photophysical properties of **1** are compiled in Table 1. As is evident from this table, the main absorption band—attributed to the 0−0 vibrational band of a strong S_0-S_1 transition—is centered between 593 and 610 nm in the pure solvents (1−18). In cyclohexane, methylcyclohexane, tetrahydrofuran (THF), toluene, diethyl ether, diisopropyl ether, and dibutyl ether, a shoulder at the short wavelength (high-energy) side can be observed—centered at approximately 565 nm—which is assigned to the 0−1 vibrational band of the same transition. In addition, weaker absorption bands are found at approximately 425 and 375 nm, the position of which is not appreciably affected by solvent polarity. These broader and weaker absorption bands are assigned to the S_0-S_2 and S_0-S_3 transitions. The position of the S_0-S_1 absorption band shows minor solvent-dependent shifts, indicating a weak charge-transfer character for the lowest electronic excitation in the ground-state geometry, vide infra. The typical, narrow BODIPY-like main absorption band[5,13−23] of **1** is, however, only seen in cyclohexane and methylcyclohexane. The full width at half-maximum ($fwhm_{abs}$) increases from 938 cm^{-1} in methylcyclohexane to 1902 cm^{-1} in THF. The fluorescence excitation spectra match the absorption spectra.

Conversely, the fluorescence emission of **1** is strongly solvent dependent. The emission maximum steadily shifts to longer wavelengths in going from nonpolar to polar solvents (from 612 nm in cyclohexane and methylcyclohexane to 737 nm in DMSO), indicative of the charge transfer nature of the emitting state. This red shift is accompanied by a loss of fine structure and an increase of the bandwidth. Only the emission spectrum in cyclohexane and methylcyclohexane displays the typical BODIPY features,[5,13−23] i.e., a narrow, slightly Stokes-shifted band of mirror image shape.

Examination of the chemical structure of **1** suggests that the occurrence of an intramolecular charge transfer (ICT) process may be responsible for its high solvent sensitivity: the tertiary amino group is an electron donor and the boradiazaindacene moiety is electron-deficient, allowing for the occurrence of an excited state with some ICT character.

Figure 2 shows the delocalized forms that contribute to the real structure of **1** in a valence bond picture. Zwitterionic structures A and B[23] have dominant contributions to both the ground (S_0) and the excited (S_1) state in the BODIPY chromophore. These structures will also be the main contributors to the ground state of **1**, thereby rationalizing the slight sensitivity of the absorption peak with solvent polarity/polarizability. In the excited state, however, a larger weight is expected for the charge-separated structure C. This is confirmed by the quantum-chemical calculations (see below) and is enhanced by the geometric deformations in the relaxed excited state (which lead to an increased "quinoid" character of the styryl side chain, hence further favoring the charge-separated form C). As a result, a difference in dipole moment between the ground and excited states develops after geometric relaxation in the excited state, such that polar, nonprotic solvents stabilize the excited state and lead to a red-shifted emission.

This also implies that, in the relaxed excited-state geometry (with a larger contribution of structure C), the nitrogen lone pair is less available for hydrogen bonding with a protic solvent. Hence, interaction between hydrogen donating solvents and the aniline nitrogen are expected to be weaker in the excited state than in the ground state, so that hydrogen bonding should

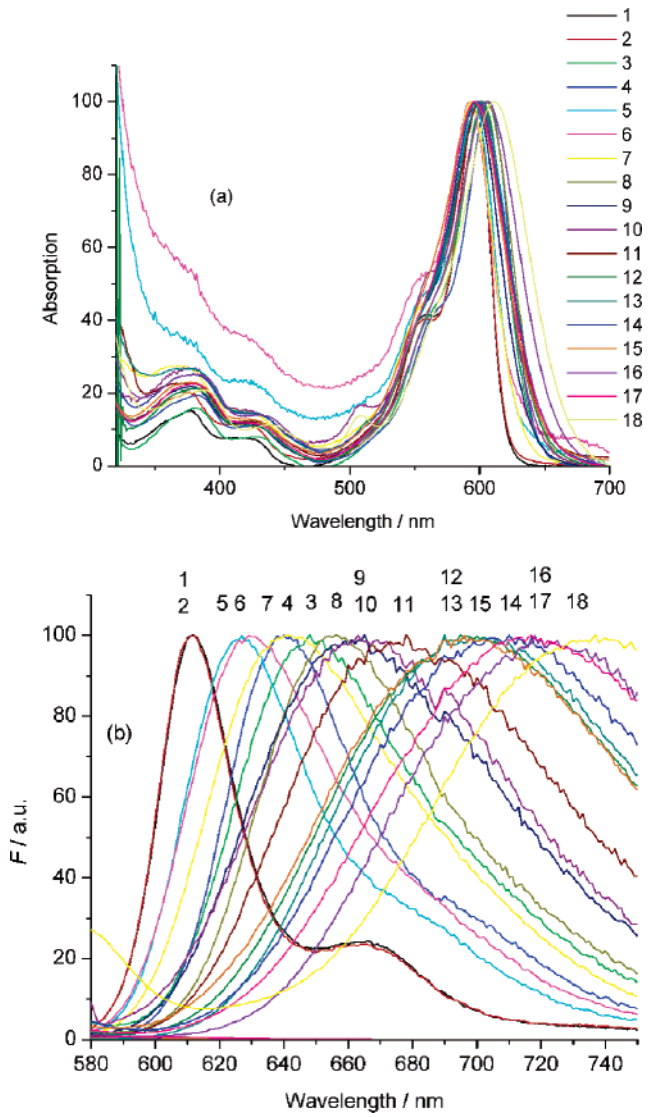

Figure 1. Normalized absorption (a) and emission spectra (b) of **1** (at λ_{ex} = 560 nm) in several solvents. The numbers refer to the solvents of Table 1: 1 = methylcyclohexane, 2 = cyclohexane, 3 = 1,4-dioxane, 4 = toluene, 5 = dibutyl ether, 6 = diisopropyl ether, 7 = diethyl ether, 8 = chloroform, 9 = ethyl acetate, 10 = tetrahydrofuran (THF), 11 = 1-butanol, 12 = acetone, 13 = butanenitrile (butyronitrile), 14 = propanenitrile (propionitrile), 15 = methanol, 16 = *N*,*N*-dimethylformamide (DMF), 17 = acetonitrile, 18 = dimethyl sulfoxide (DMSO).

TABLE 1: Photophysical Properties of 1 in Several Solvents[a]

no.	solvent	λ_{abs} (max/nm)	λ_{em} (max/nm)	λ_{ex} (max/nm)	$\Delta\bar{\nu}$ (cm^{-1})	$fwhm_{abs}$ (cm^{-1})	ϕ_f	τ_1 (ns)	τ_2 (ps)	k_f ($10^8\ s^{-1}$)	k_{nr} ($10^8\ s^{-1}$)
1	methylcyclohexane	597	612	597	411	938	0.86 ± 0.02				
2	cyclohexane	597	612	597	411	968	0.97 ± 0.03	3.50		2.77	0.09
3	1,4-dioxane	602	648	602	1179	1370	0.77 ± 0.06	3.43		2.24	0.67
4	toluene	607	640	607	850	1267	0.85 ± 0.02	3.25		2.62	0.46
5	dibutyl ether	596	627	596	830	1350	0.91 ± 0.02				
6	diisopropyl ether	594	629	594	937	1512	0.87 ± 0.03				
7	diethyl ether	593	641	593	1263	1444	0.93 ± 0.02	3.74		2.49	0.19
8	choroform	605	656	605	1285	1620	0.82 ± 0.04	3.47		2.36	0.52
9	ethyl acetate	596	665	596	1741	1513	0.59 ± 0.01	3.31		1.78	1.24
10	THF	600	664	600	1606	1902	0.56 ± 0.04	3.00		1.87	1.47
11	1-butanol	601	678	601	1890	1730	0.59 ± 0.03	2.45	106		
12	acetone	597	695	597	2362	1648	0.27 ± 0.01	2.23		1.21	3.27
13	butanenitrile	600	695	600	2278	1725	0.27 ± 0.02	2.26		1.19	3.23
14	propanenitrile	598	710	598	2638	1762	0.19 ± 0.03	1.84		1.03	4.40
15	methanol	596	696	598	2411	1838	0.16 ± 0.01	0.85	14		
16	DMF	607	718	607	2547	1827	0.08 ± 0.01				
17	acetonitrile	597	717	597	2803	1762	0.090 ± 0.002	1.20		0.75	7.58
18	DMSO	610	737	609	2825	1876	0.056 ± 0.007				
19	$CH_3CN + H^+$	553	561	553	258	725	1.00 ± 0.02	4.19		2.39	0

[a] For the time-resolved fluorescence measurements, the samples in solvents 2−4, 7−15, and 17 were excited at 580 nm whereas 530 nm excitation was used for solvent 19. For the steady-state and time-resolved fluorescence measurements in solvent 19, $HClO_4$ was used as proton source. The standard errors on τ_1 are ≤ 15 ps and ≤ 3 ps on τ_2. ϕ_f values were determined by excitation at 560 nm (1−18) and 530 nm (19).

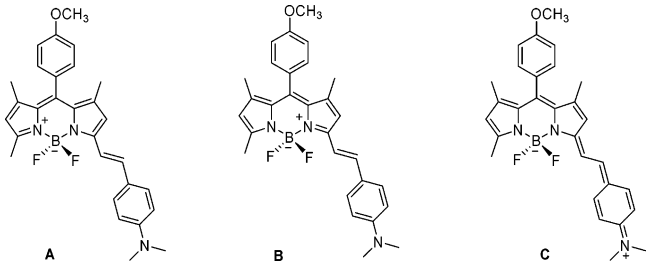

Figure 2. Delocalized structures of **1** contributing to its real structure in the ground and excited states.

stabilize the ground state more than the excited state. This should shift the emission to shorter wavelengths compared to a nonprotic solvent with the same dielectric constant.

The results of time-resolved fluorescence experiments are also listed in Table 1. In all pure nonprotic solvents studied, a single decay component on the nanosecond time scale was found, ranging from 3.74 ns in diethyl ether to 1.20 ns in acetonitrile, analogous to the borondipyrromethene derivative 3-{2-[4-(dimethylamino)phenyl]ethenyl}-8-phenyl-1,5,7-trimethyl borondipyrromethene.[17] In addition, in the protic solvents (methanol and 1-butanol), a second, faster subnanosecond component of 14 and 106 ps, respectively, was found. The time-resolved fluorescence profiles of **1** in methanol were measured at λ_{em} = 640, 655, 670, 700, and 730 nm. In 1-butanol, six emission wavelengths were used (λ_{em} = 625, 640, 655, 670, 700, and 730 nm). The collected fluorescence decay surfaces were analyzed globally as biexponentials with linked decay times τ_1 (slow) and τ_2 (fast). In methanol, the relative preexponential factor α_2 associated with the fast decay component (τ_2) decreased with increasing detection wavelength λ_{em} (α_2/α_1 = 2.17, 1.30, 0.84, and 0.17 at 640, 655, 670, and 700 nm, respectively) and became negative at the longest wavelength ($\alpha_2/\alpha_1 = -0.10$ at 730 nm). Similar observations were made in 1-butanol: $\alpha_2/\alpha_1 = 3.03$ at 625 nm, decreasing to 1.96, 0.90, and 0.37 at 640, 655, and 670 nm, respectively, and becoming progressively more negative at longer λ_{em} ($\alpha_2/\alpha_1 = -0.27$ at 700 nm and $\alpha_2/\alpha_1 = -0.68$ at 730 nm). This fast component is observed in methanol and not in nonprotic polar solvents as THF, ethyl acetate, or dioxane, which have a similar viscosity. Therefore, it is more likely to be due to a rearrangement of the hydrogen bond after excitation rather than to a dipolar reorientation of the solvent or relaxation of the molecular geometry. We did not attempt to further investigate the nature of this component, but we attribute it to the dynamics of hydrogen bonding of the alcohol to the amine group after electron transfer. Since in structure C (Figure 2) a positive charge is present on the aniline nitrogen, the rearrangement of the hydrogen bond must correspond to a weakening of the hydrogen bond between the solvent and the aniline nitrogen after excitation. A weaker hydrogen bond will make the amine a better donor and lower the energy of the ICT-like excited state, leading to a bathochromic shift of the emission on a time scale of a few picoseconds,[25,26] consistent with our observations. At shorter λ_{em}, the emission originates mainly from a hydrogen-bonded ICT state, which evolves into a nonhydrogen-bonded ICT state emitting at longer λ_{em} (hydrogen bonding decreases the electron donor capacity of the aniline nitrogen and hence leads to a hypsochromic shift). This is consistent with the weaker interaction between the hydrogen donating solvents and the aniline nitrogen in the excited state compared to the ground state, as discussed above.

The larger value of the fast decay time τ_2 in 1-butanol might be due to the higher viscosity of this solvent, and is somewhat faster than the time scale measured for solvation dynamics in other more viscous long-chain alcohols such as 1-decanol (~500 ps).[27] It is unlikely that the difference of τ_2 between methanol and 1-butanol is related to a difference in solvent polarity. A lower-polarity solvent such as 1-butanol (dielectric constant ϵ = 17.1 compared to 32.6 for methanol) will lead to a less extensive bathochromic shift by dipolar interactions. This would slow the relaxation, and even longer relaxation times would be observed in solvents such as THF (ϵ = 7.4 and diethyl ether, ϵ = 4.3). This is, however, not the case. Conversely, a higher viscosity will slow the dipolar relaxation of the solvent by increased friction forces. Furthermore, the oxygen of 1-butanol competes more efficiently than the oxygen of methanol with the aniline nitrogen of BODIPY **1** for protons. Hence, one can also expect a less important hydrogen bonding in 1-butanol leading again to a smaller red shift due to a rearrangement of the hydrogen bond after excitation. As the solvent relaxation involves a weakening of the hydrogen bond after excitation (see

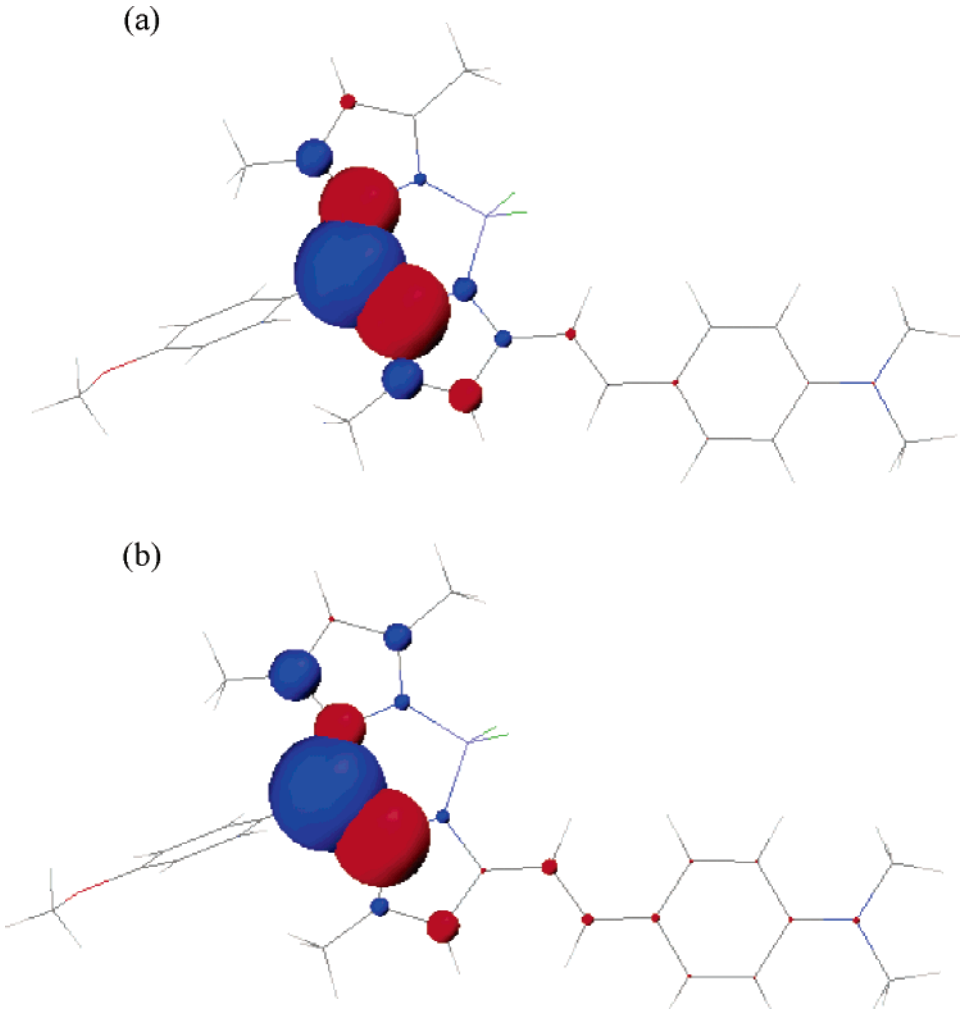

Figure 3. Schematic representation of the changes in charge distribution between the ground state and the excited state, as computed at the INDO/SCI level on the basis of the ground-state (a) and excited-state (b) geometry.

above), it is difficult to understand why this should be slowed in the less polar 1-butanol where a less extensive rearrangement is necessary. However, the difference in viscosities (0.597 cP in methanol and 2.95 cP in 1-butanol) can explain why the rearrangement of this hydrogen bond after excitation is slower in 1-butanol.

2.3. Solvatochromic Effects. At the simplest level, solvent-dependent shifts of the fluorescence emission spectra are interpreted in terms of the Lippert−Mataga equation (eq 7, theoretical section), which describes the Stokes shift ($\Delta\bar{\nu} = \bar{\nu}_{abs} - \bar{\nu}_{em}$) as a function of the interaction between the change of the dipole moment of **1** upon excitation, and the dipole in solvents with different dielectric constants (ϵ) and refractive indices (n).[28, 29]

The use of eq 7 is limited to transitions where the excited-state reached after absorption is also the emissive state (hence for $S_0 \rightarrow S_1$ excitation and identical dipole moments for the Franck−Condon and relaxed excited states) and where the excited-state dipole moment is independent of solvent polarity. To go beyond the limitations imposed by the Lippert model, INDO/SCI calculations are presented here, in which self-consistent reaction field (SCRF) calculations are performed for pairs of states (ground state + excited state) considering full (i.e., electronic and inertial) relaxation in the initial state and only electronic relaxation in the final state (see Theoretical Section). The interaction between the final state and the mean reaction field created by the initial state leads to expressions similar to eqs 4 and 5 for a spherical cavity with radius a (but where the excitation energies and dipoles are obtained at the output of a SCRF process).[30] From the molar mass of **1** and assuming a density of 1 g/cm^3, a radius $a \approx 5.8$ Å was inferred. This is, however, an upper limit for a, because the corresponding molar volume includes space between spheres and this space is expected to be filled with solvent. An alternative is to describe the solute on the basis of inscribed cubes,[30] which leads to $a \approx 4.8$ Å. Here, we have adopted an intermediate value a of 5.25 Å that provides well-converged SCRF properties for all solvents considered[31] and spectral shifts in reasonable agreement with experiment.

The INDO/SCI calculations indicate a significant increase in the vertical dipole moment difference $\Delta\vec{\mu}_{ge}$when going from the (AM1/CAS-CI) ground-state equilibrium geometry (i.e., initial state for absorption) to the excited-state geometry (initial state for emission); in the gas phase, these values amount to ∼2.6 and ∼7.3 D, respectively. This is illustrated in Figure 3, displaying the changes in charge distribution between the ground and excited states, as obtained from a ZDO (zero differential overlap) analysis on both geometric structures. Although the excited-state wave function (the differential density between S_0 and S_1; see Figure 3) is still mostly confined on the BODIPY core, larger contributions on the *p*-*N*,*N*-dimethylaminostyryl side chain are computed in the excited-state configuration. These are consistent with increased charge-transfer contributions and, therefore, also a larger permanent dipole in the excited state.

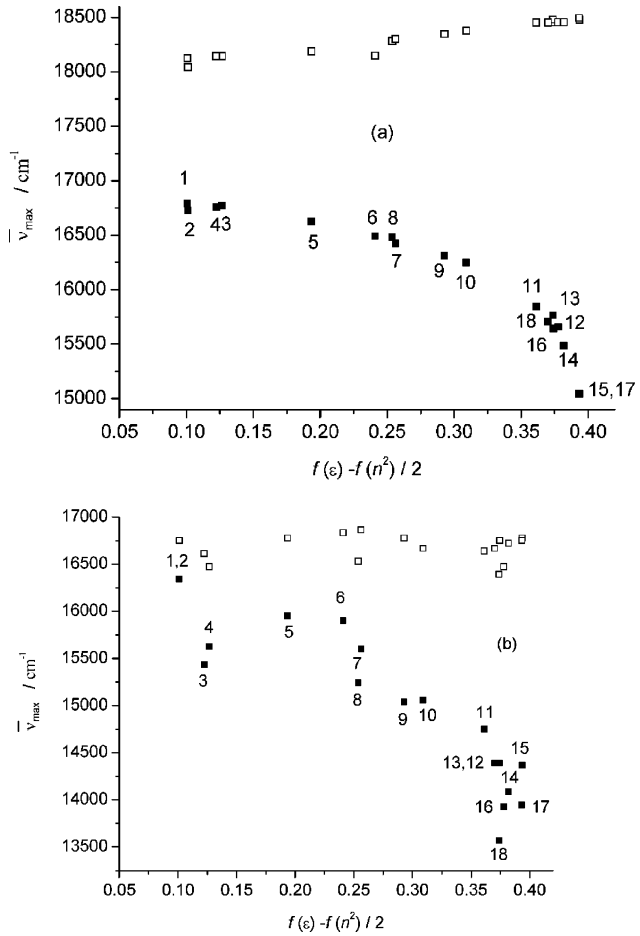

Figure 4. Plots of the absorption ($\bar{\nu}_{abs}$, open squares) and emission ($\bar{\nu}_{em}$, filled squares) maxima (in cm^{-1}) of **1**: (a) calculated at the INDO/SCI level and (b) measured by steady-state spectroscopy in solvents (1−18) vs [$f(\epsilon) - {}^1/_2\, f(n^2)$]. The numbers refer to the same solvents as in Figure 1 and Table 1.

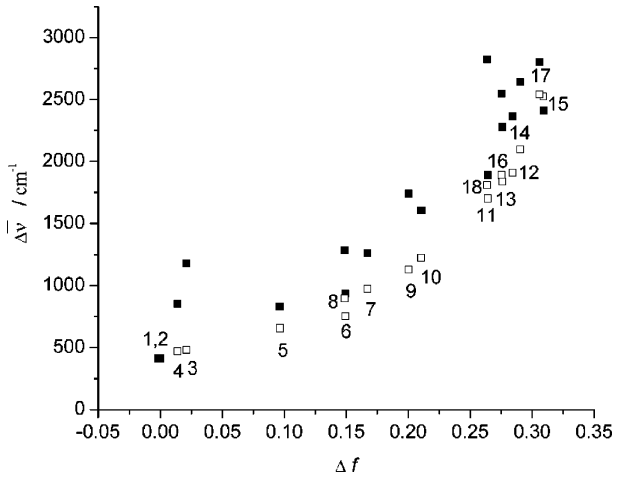

Figure 5. Plots of the Stokes shifts ($\Delta\bar{\nu}$) (in cm^{-1}) of **1,** calculated at the INDO/SCI level (open squares) and measured by steady-state spectroscopy (filled squares) in solvents (1−18) vs the Lippert solvent parameter $\Delta f = f(\epsilon) - f(n^2)$. The calculated and experimental data for solvents 1 and 2 overlap. The numbers refer to the same solvents as in Figure 1 and Table 1.

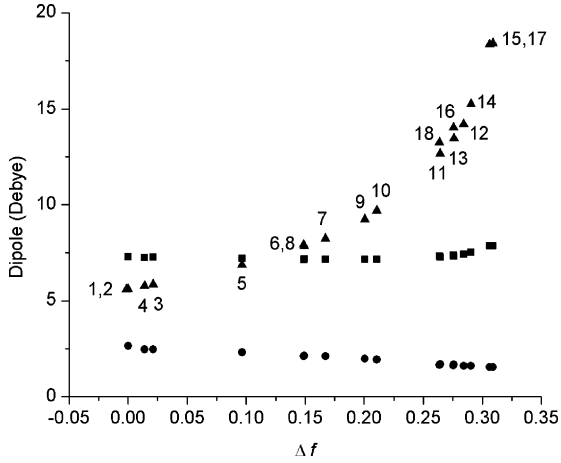

Figure 6. Plots of the vertical dipole moment differences in the ground $|\Delta\bar{\mu}_{ge}(G)|$ (circles) and excited $|\Delta\bar{\mu}_{ge}(E)|$ (squares) state geometries and the adiabatic $|\Delta\bar{\mu}_{ge}(ad)|$ (triangles) dipole moment difference in solvents (1−18) vs the Lippert solvent parameter Δf. The numbers refer to the same solvents as in Figure 1 and Table 1.

As a consequence of the reshuffling in charge density upon electronic excitation, the ground-state vertical absorption is very slightly (blue) shifted with increasing solvent polarity (in the ground-state geometry, we have $|\bar{\mu}_g(G)| \approx |\bar{\mu}_e(G)|$ and the spectral shift mostly arises from solvent polarizability), while the excited-state vertical emission is strongly red-shifted (in the excited-state geometry, we have $|\bar{\mu}_e(E)| \gg |\bar{\mu}_g(E)|$), see Figure 4. The asymmetric evolution of the spectral shifts in absorption and emission predicted on the basis of the INDO/SCI results is fully supported by the experimental data (compare parts a and b of Figure 4).

Interestingly, both theory and experiment yield a poor linear relationship of the Stokes shift $\Delta\bar{\nu}$ vs Δf (Figure 5). This arises primarily from the nonlinear evolution of the Stokes shift in the more polar solvents, that is for $\Delta f \geq 0.2$.

To rationalize this evolution, it is useful to look at the relevant state dipole moment differences, namely $|\Delta\bar{\mu}_{ge}(G)|$, $|\Delta\bar{\mu}_{ge}(E)|$, and $|\Delta\bar{\mu}_{ge}(ad)|$(the difference between the dipoles in the relaxed ground and excited states, i.e., the "adiabatic" dipole moment difference) (see Figure 6). The vertical dipole differences $|\Delta\bar{\mu}_{ge}(G)|$ and $|\Delta\bar{\mu}_{ge}(E)|$ show hardly any dependence on solvent polarity, while the adiabatic quantity $|\Delta\bar{\mu}_{ge}(ad)|$ increases significantly in more polar solvents (for Δf values larger than $\sim$ 0.15). For compound **1**, it turns out that: $|\Delta\bar{\mu}_{ge}(E)| \gg |\Delta\bar{\mu}_{ge}(G)|$. In addition, $|\bar{\mu}_e(E)| \approx |\Delta\bar{\mu}_{ge}(E)|$ for small Δf values ($<$0.15). (In more polar solvents the ground-state dipole becomes significant.) When only the (dominant) contribution from emission to the Stokes shift is retained, eqs 4 and 5 can then be combined into the Lippert−Mataga expression (eq 7), but where $\Delta\bar{\mu}_{ge}$ is the dipole difference computed in the excited-state equilibrium geometry. The best linear fit of the measured Stokes shift $\Delta\bar{\nu}$ in the solvent polarity range ($0 < \Delta f < 0.15$) (Figure 5) yields $\Delta\bar{\mu}_{ge}(E) \approx 7.4$ D for $a = 5.25$ Å, in excellent agreement with the calculated value (Figure 6). For more polar solvents, $\bar{\mu}_e(E)$ and $\Delta\bar{\mu}_{ge}(ad)$ increase substantially, the dependence of the Stokes shift $\Delta\bar{\nu}$ on Δf is nonlinear and eq 7 fails to reproduce the experimental data. The more pronounced evolution of $\bar{\mu}_e(E)$ with Δf (as compared to $\bar{\mu}_g(G)$) and the resulting increase in $\Delta\bar{\mu}_{ge}(ad)$ [and to a lesser extent $\Delta\bar{\mu}_{ge}(E)$] likely arise from the larger polarizability of **1** in its excited state. In the SCRF procedure applied here, the total dipole of the solute molecule in a given excited state is the sum of the source (initial) dipole and an induced contribution associated with the solvent reaction field. As the latter contribution is proportional to the polarizability (α) of the solute in that state, a larger induced dipole in the excited state follows from $\alpha_e > \alpha_g$. Although we did not pursue this further, we note that expressions for the

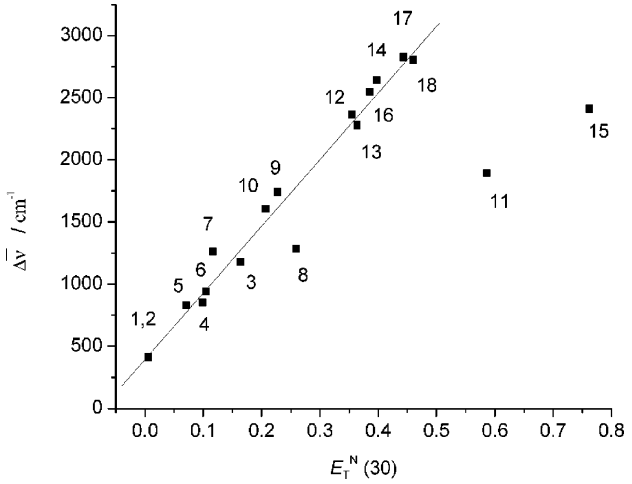

Figure 7. Stokes shift ($\Delta\bar{\nu}$) (in cm^{-1}) of **1** as a function of the solvent polarity parameter $E_T^N(30)$. The numbers refer to the same solvents as in Figure 1 and Table 1. The straight line is the best linear fit (r = 0.982) for the nonprotic solvents (i.e., excluding methanol and 1-butanol).

spectral shifts accounting for such changes in polarizability between ground and excited state have been derived.[32,33]

While the Lippert solvent parameter Δf only considers the permanent dipole moment and to some extent the polarizability of the solvent, other solvent polarity scales—e.g., the normalized $E_T^N(30)$ scale[34]—used to describe the solvatochromic shifts observed in the absorption and fluorescence spectra also take into account the hydrogen bond donating and accepting character of the solvent. Figure 7 shows the Stokes shift $\Delta\bar{\nu}$ of **1** as a function of the $E_T^N(30)$ solvent parameter. From this figure, two different groups of solvents can be distinguished: nonprotic and protic (methanol and 1-butanol) solvents. There is an adequate linear relationship ($r = 0.982$) between the Stokes shift and the $E_T^N(30)$ polarity scale for the nonprotic solvents (i.e., excluding methanol and 1-butanol). A similar linear relationship ($r = 0.984$) was found between the fluorescence emission maximum $\bar{\nu}_{em}$ and $E_T^N(30)$ for the nonprotic solvents. For the protic solvents methanol and 1-butanol, the Stokes shift is much smaller than expected based on the $E_T^N(30)$ scale. For **1**, an increase of the permanent dipole moment of the solvent leads to a large red shift of the emission while increasing the hydrogen donating character of the solvent leads to a negligible red shift or perhaps even a blue shift of the emission from the relaxed excited state. This corresponds to our earlier discussion on the delocalized structures shown in Figure 2.

The solvent effect on $\bar{\nu}_{abs}$, $\bar{\nu}_{em}$, and the Stokes shift $\Delta\bar{\nu}$ can also be described on the basis of a multilinear expression (eq 1a):

$$y = y_0 + a\mathrm{A} + b\mathrm{B} + c\mathrm{C} \quad (1a)$$

in which y_0 stands for the physicochemical property of interest in the absence of solvent (i.e., in the gas phase); a, b, and c are adjustable coefficients that reflect the dependency of the physicochemical property (y) in a given solvent on the various (A, B, C) solvent parameters. At least two different sets of solvent scales can be found in the literature to characterize these solvent properties. In the present analysis, the polarity/polarizability, the acidity, and the basicity of the solvent are taken into account. Kamlet and Taft[35] put forward the π^*, α, and β parameters to characterize, respectively, the polarity/polarizability, the acidity, and the basicity of a solvent (eq 1b). Conversely, Catalán et al. proposed empirical solvent scales for polarity/polarizability (SPP[36,37]), for acidity (SA[37]), and for basicity (SB[37,38]) to describe the respective properties of a given solvent (eq 1c). The essential difference between the two sets of scales lies in the fact that the Catalán scales have been constructed with data obtained from the same laboratory, by using always the adequate probe/homomorph pair, and therefore, these scales represent the corresponding pure effects. The data values from the scales by Kamlet and Taft, however, have in many cases been obtained from an average of about 40 probes, measured by different authors from several laboratories.

$$y = y_0 + a_\alpha\alpha + b_\beta\beta + c_{\pi^*}\pi^* \quad \text{(Kamlet–Taft)} \quad (1b)$$

$$y = y_0 + a_{SA}\mathrm{SA} + b_{SB}\mathrm{SB} + c_{SPP}\mathrm{SPP} \quad \text{(Catalán)} \quad (1c)$$

Table 2 lists the estimated coefficients y_0, a, b, c (see eq 1) and correlation coefficients (r) for the multiple linear regression analysis of the absorption ($\bar{\nu}_{abs}$) and fluorescence emission maxima ($\bar{\nu}_{em}$), and the Stokes shift $\Delta\bar{\nu}$ of **1** as a function of the Kamlet–Taft (eq 1b) and Catalán (eq 1c) solvent scales for the pure solvents (1–18 of Table 1). The Kamlet–Taft solvatochromic parameters α, β, and π^* parameters are taken from ref 39, while the Catalán solvent parameters SA, SB, and SPP are from refs. 36–38. Both sets of solvent scales produce similar qualitative results, although the Catalán scales yields somewhat better fits for $\bar{\nu}_{em}$ and $\Delta\bar{\nu}$ (as judged by the correlation coefficient r as goodness-of-fit criterion).

The correlation coefficients (r) for the multilinear fits of the absorption maxima of **1** vs solvent polarity/polarizability, acidity, and basicity are far from 1.0. However, there is a linear relationship between $\bar{\nu}_{abs}$ and the Catalán solvent polarizability parameter SP (see below). Conversely, much better r values

TABLE 2: Estimated Coefficients (y_0, a, b, c; See Eq 1) and Their Standard Errors and Correlation Coefficients (r) for the (Multiple) Linear Regression Analysis of the Absorption ($\bar{\nu}_{abs}$) and Fluorescence Emission Maxima ($\bar{\nu}_{em}$), and the Stokes Shift $\Delta\bar{\nu} = \bar{\nu}_{abs} - \bar{\nu}_{em}$ of 1 in Solvents 1–18 (Table 1) as a Function of the Catalán (eq 1c; Acidity SA, Basicity SB, and Polarity/Polarizability SPP) and Kamlet–Taft (eq 1b; Acidity α, Basicity β, and Polarity/Polarizability π^*) Solvent Scales

Catalán	y_0 (cm^{-1})	a_{SA}	b_{SB}	c_{SPP}	r
$\bar{\nu}_{abs}$	$(17.0 \pm 0.2) \times 10^3$	$(1 \pm 2) \times 10^2$	$(2 \pm 2) \times 10^2$	$(-5 \pm 3) \times 10^2$	0.505
$\bar{\nu}_{em}$	$(20.0 \pm 0.3) \times 10^3$	$(-3 \pm 3) \times 10^2$	$(4 \pm 2) \times 10^2$	$(-6.5 \pm 0.4) \times 10^3$	0.978
$\bar{\nu}_{em}$	$(20.0 \pm 0.3) \times 10^3$			$(-6.3 \pm 0.4) \times 10^3$	0.973
$\Delta\bar{\nu}$	$(-2.9 \pm 0.4) \times 10^3$	$(4 \pm 4) \times 10^2$	$(-2 \pm 3) \times 10^2$	$(6.0 \pm 0.5) \times 10^3$	0.962
Kamlet–Taft	y_0 (cm^{-1})	a_α	b_β	c_{π^*}	r
$\bar{\nu}_{abs}$	$(16.8 \pm 0.1) \times 10^3$	$(1 \pm 1) \times 10^2$	$(2 \pm 2) \times 10^2$	$(-3 \pm 1) \times 10^2$	0.631
$\bar{\nu}_{em}$	$(16.6 \pm 0.2) \times 10^3$	$(-4 \pm 3) \times 10^2$	$(-3 \pm 4) \times 10^2$	$(-2.7 \pm 0.3) \times 10^3$	0.947
$\bar{\nu}_{em}$	$(16.5 \pm 0.2) \times 10^3$			$(-2.9 \pm 0.3) \times 10^3$	0.929
$\Delta\bar{\nu}$	$(2 \pm 2) \times 10^2$	$(4 \pm 3) \times 10^2$	$(5 \pm 5) \times 10^2$	$(2.4 \pm 0.4) \times 10^3$	0.912

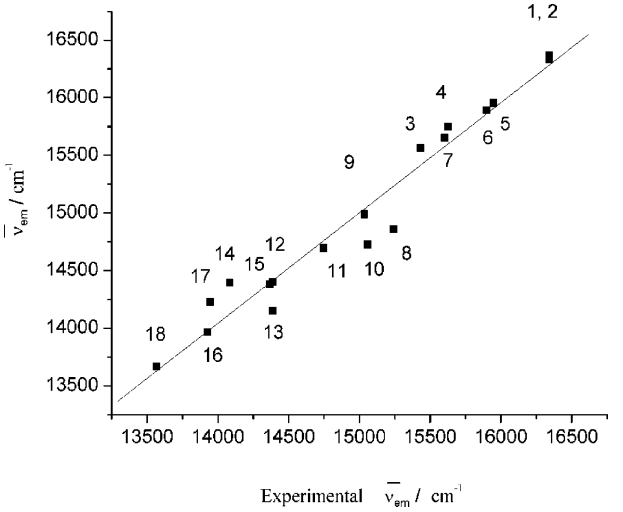

Figure 8. Linear relationship ($r = 0.978$) between the experimental and predicted fluorescence emission maxima $\bar{\nu}_{em}$ (in cm^{-1}) of **1** obtained by a multiple linear regression analysis according to eq 1c in which y_0, and the Catalán solvent polarity/polarizability (a_{SPP}), the acidity (b_{SA}), and basicity (c_{SB}) coefficients are estimated simultaneously. The numbers refer to the same solvents as in Figure 1 and Table 1.

are found for the multilinear fitting of the fluorescence emission maxima $\bar{\nu}_{em}$. For both sets of solvent scales, the estimated coefficients describing the solvent polarity/polarizability (large and negative c_{SPP} and c_π* values) indicate that the solvent polarity/polarizability is the main parameter responsible for the shift of the fluorescence emission band ($\bar{\nu}_{em}$) to lower energies, corroborating the observed bathochromic shifts of the emission maximum $\bar{\nu}_{em}$with higher [$f(\epsilon) - {}^1/_2\, f(n^2)$] (see Figure 4). The (absolute) values of the coefficients a_{SA} and b_{SB} are indeed much smaller than c_{SPP}. The same is true for a_α and b_β compared to c_π*. Furthermore, for the fits of $\bar{\nu}_{em}$, the standard errors on the parameters a_{SA} and b_{SB} (and a_α and b_β) are of comparable magnitude as the parameters themselves. The errors on y_0, c_{SPP}, and c_π*, however, are much smaller. Fitting a linear equation with the solvent scale SPP as the only independent variable to $\bar{\nu}_{em}$ (eq 1b with $a_{SA} = 0$ and $b_{SB} = 0$) confirms that the polarity/polarizability of the solvent is the most important factor determining the fluorescence emission maximum. Indeed, this linear fit (Catalán, Table 2) has a similar r value (0.973) as the multilinear fit ($r = 0.978$). An analogous result is obtained for the Kamlet−Taft scale: if the solvent parameter π* is used as the only independent variable in the linear equation to fit $\bar{\nu}_{em}$ (eq 1c with $a_\alpha = 0$ and $b_\beta = 0$), the obtained correlation coefficient ($r = 0.929$) is somewhat smaller than for the multilinear fit ($r = 0.947$).

Figure 8 shows the relationship between the fluorescence maxima ($\bar{\nu}_{em}$) predicted by the multicomponent linear regression using the estimated a_{SA}, b_{SB}, and c_{SPP} coefficients (Catalán scale, eq 1c) vs the respective experimental values. There is a linear relationship encompassing *all* solvents (1−18), corroborating the high correlation coefficient found for the multilinear Catalán fit. An analogous curve of $\bar{\nu}_{em}$ for the Kamlet−Taft solvent scales (figure not shown) indicates that the Kamlet−Taft scales is slightly less appropriate than the Catalán scales for describing the solvent dependent fluorescence emission shifts of **1**.

The small solvatochromism of **1** for absorption is noteworthy. Indeed, the data of Table 2 indicate that $\bar{\nu}_{abs}$ does not depend on solvent polarity/polarizability, acidity, or basicity. However, this small change may reflect just a slight change in polarizability on the environment of the chromophore. Indeed, when one plots $\bar{\nu}_{abs}$ as a function of the Catalán solvent polarizability

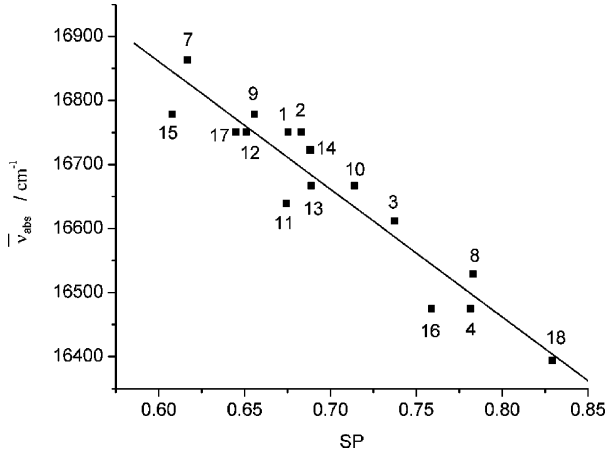

Figure 9. Linear relationship ($r = -0.948$) of the experimental $\bar{\nu}_{abs}$ (in cm^{-1}) of **1** vs the Catalán solvent polarizability parameter SP. The numbers refer to the same solvents as in Figure 1 and Table 1.

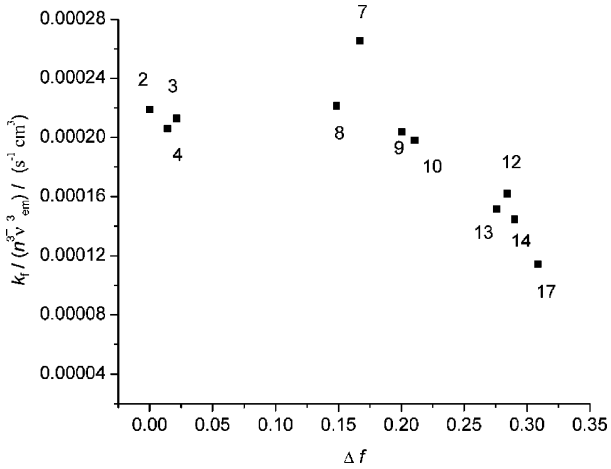

Figure 10. Plot of $k_f/(n^3\bar{\nu}_{em}{}^3)$) vs Δf for **1**. The numbers refer to the same solvents as in Figure 1 and Table 1.

parameter SP (SP[40] scale) for 16 solvents of Table 1 [the SP values for dibutyl ether (solvent 5) and diisopropyl ether (solvent 6) are not available right now], an excellent linear relationship (eq 2, $r = -0.948$) is found between $\bar{\nu}_{abs}$ and SP (Figure 9),

$$\bar{\nu}_{abs} = \bar{\nu}_{abs}{}^0 + a_{SP}\mathrm{SP} \qquad (2)$$

with $\bar{\nu}_{abs}{}^0 = (18.1 \pm 0.1) \times 10^3$ cm^{-1} and $a_{SP} = (20 \pm 2) \times 10^2$. This clearly indicates that the absorption spectra depend only on the change of polarizability of the environment of the chromophore.

Using the fluorescence decay time τ and the fluorescence quantum yield ϕ_f, the rate constants for fluorescence (k_f) and nonradiative decay (k_{nr}) can be calculated according to eq 9 (see Experimental Section). The data in Table 1 show that k_f decreases with increasing solvent polarity. Since k_f is proportional to the product of the squared transition dipole moment $\langle\psi_G|\hat{\mu}|\psi_E\rangle^2$, n^3, and $\bar{\nu}_{em}{}^3$ (eq 3),[41]

$$k_f = \frac{64\pi^4}{3h} n^3 \bar{\nu}_{em}{}^3 \langle\psi_G|\hat{\mu}|\psi_E\rangle^2 \qquad (3)$$

we plotted $k_f/(n^3\bar{\nu}_{em}{}^3)$ of **1** vs Δf in Figure 10. In eq 3, $\hat{\mu}$ stands for the dipole moment operator. This ratio remains practically constant up to $\Delta f \approx 0.20$ and then decreases with increasing Δf to reach about half its value in acetonitrile compared to the apolar solvents. This means that the transition dipole moment

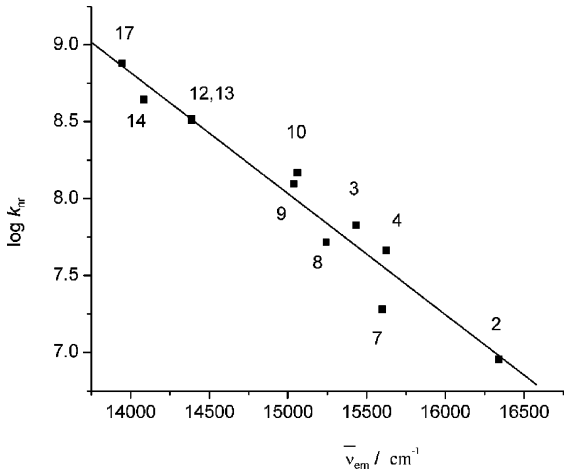

Figure 11. Plot of log (k_{nr}/s^{-1}) vs $\bar{\nu}_{em}$ (in cm^{-1}) for **1**. The numbers refer to the same solvents as in Figure 1 and Table 1. The straight line is the best linear fit ($r = -0.974$) to the data.

$\langle\psi_G|\hat{\mu}|\psi_E\rangle$ has decreased by 30%. This corresponds to the increase of the excited-state dipole moment in more polar solvents as suggested by the nonlinear Lippert−Mataga plot (Figure 5) and theoretical calculations.[42]

The strong increase of k_{nr} upon increasing solvent polarity (Figure 11) can be rationalized if k_{nr} can be attributed mainly to internal conversion. This nonradiative transition is accompanied by a large change in dipole moment. Although there is no full electron transfer as in exciplexes,[43] the nonradiative processes can be considered to be due to some extent to a partial charge transfer between the strongly coupled BODIPY and aniline moieties. The free energy dependence of the rate of charge transfer is currently described in Marcus' theory.[44] In the framework of this theory, the solvation will act as accepting modes for this internal conversion process.[45] The energy gap between the singlet excited state and the ground state is, in all solvents, close to or above 2 eV; thus, it always exceeds the reorganization energy, and the nonradiative process proceeds in the "inverted" region.[46] Increasing the solvent polarity decreases the energy gap and simultaneously increases the reorganization energy. In the "inverted" region, both factors will increase the rate of the nonradiative process. As the increased value of k_{nr} can be rationalized in the framework of Marcus' theory, the effect of the changing electronic structure in more polar solvents is apparently less relevant than for k_f.

2.4. pH Dependence of the Absorption and Fluorescence Spectra in Acetonitrile Solution. Protonation of the tertiary amine function drastically alters the electron-donating properties of the tertiary amine group and consequently is expected to switch off the ICT to the borondipyrromethene moiety. In acidified acetonitrile, this produces the typical BODIPY-like narrow absorption and emission bands with a very high fluorescence yield.[5,13−23] The absorption spectra of **1** in acetonitrile are shown as a function of pH in Figure 12a. The absorption spectra of **1** show a decrease of the absorbance band with a maximum at 597 nm with increasing HCl concentration (i.e., lower pH) and a simultaneous increase of the absorption at 553 nm. Varying the pH also gives rise to several isosbestic points (at 566, 465, 336, and 280 nm). The lowest-energy absorption band of the ammonium form of the dye is blue-shifted by about 40 nm in comparison to that of the neutral amine form. The width of the absorption band of the neutral amine (fwhm$_{abs}$ = 1794 cm^{-1}) is ∼50% smaller in the ammonium form (fwhm$_{abs}$ = 791 cm^{-1}).

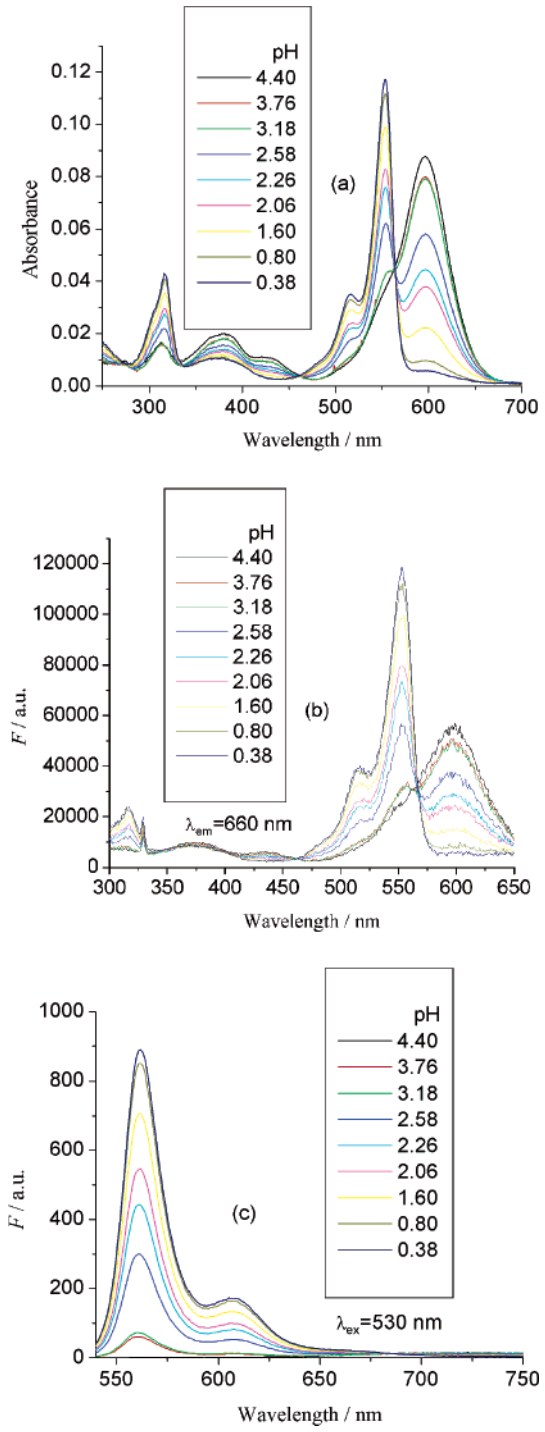

Figure 12. (a) Absorption spectra of **1** in acetonitrile solution as a function of pH. (b) Corresponding fluorescence excitation spectra (λ_{em} = 660 nm). (c) Corresponding emission spectra (λ_{ex} = 530 nm).

The fluorescence excitation (λ_{em} = 660 nm) and emission spectra (λ_{ex} = 530 nm) of **1** in acetonitrile are shown as a function of pH in Figure 12, parts b and c, respectively. The fluorescence signals increase significantly with increasing HCl concentration. In the same way as the absorption spectra, the fluorescence excitation maximum at 597 nm (neutral amine form) moves to 552 nm (positively charged ammonium form) at lower pH. The highest ϕ_f value (0.91, determined by excitation at 530 nm) is found for the ammonium form (at the lowest pH, namely 0.38). The width of the fluorescence excitation band is also reduced in going from the amine (fwhm = 1908 cm^{-1}) to the ammonium form (fwhm = 825 cm^{-1} in acidified acetonitrile), stressing the influence of the conjugated (unprotonated)

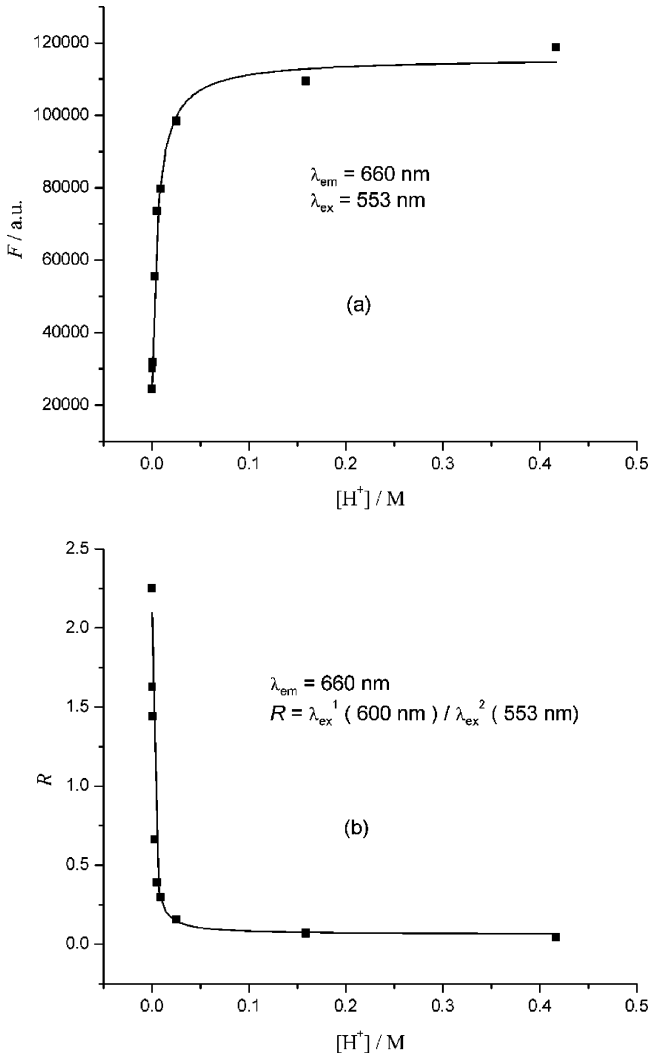

Figure 13. (a) The solid line represents the best fit of eq 10 with $n = 1$ to the *direct* excitation fluorimetric titration data of **1** obtained from the spectra of Figure 12b ($\lambda_{em} = 660$ nm, $\lambda_{ex} = 553$ nm). (b) Best fit of eq 11 with $n = 1$ to the *ratiometric* excitation fluorimetric titration data of **1** obtained from the spectra of Figure 12b ($\lambda_{em} = 660$ nm, $\lambda_{ex}^1/\lambda_{ex}^2 = 600/553$ nm).

amine group on the spectroscopic properties of **1** in solvents of any polarity. When $HClO_4$ (70% v) is added to the acetonitrile solution of **1** (pH < 0), ϕ_f increases to 1.00 and $fwhm_{abs}$ is reduced to 725 cm^{-1} (see Table 1). The apparent pH independence of the spectral shape and the maximum of the fluorescence spectra (Figure 12c) are due to the lower emission quantum yield and the small absorption coefficient of the neutral form (compared to the protonated form) at 530 nm. This elucidates the different fluorescence spectra observed in Figure 1 and in Figure 12c at pH 4.40.

The acidity constant K_a and the stoichiometry (n) of the binding of H^+ by the tertiary amine group of compound **1** were determined by fitting eq 10 or eq 11 (see Experimental Section) to the fluorescence excitation or emission spectral data.

The first method for estimating K_a and the stoichiometry (n) is the *direct* fluorimetric titration (eq 10, see Experimental Section). The results of the *direct* fluorimetric titration using the excitation data of Figure 12b ($\lambda_{em} = 660$ nm, $\lambda_{ex} = 553$ nm) are displayed in Figure 13a and yield a pK_a value of 2.27 $\pm$ 0.05 and a well-defined 1:1 stoichiometry between **1** and H^+, indicative of ammonium ion formation. A similar titration using the excitation spectra of Figure 12b ($\lambda_{em} = 660$ nm) at an excitation wavelength where the intensity decreases with lower pH ($\lambda_{ex} = 600$ nm) yields the same pK_a value (2.28 $\pm$ 0.05). These results are in perfect agreement with the curve-fittings using the absorption spectra of Figure 12a (at 552 nm: p$K_a = 2.21 \pm 0.05$, at 595 nm: p$K_a = 2.28 \pm 0.05$) and the emission spectra of Figure 12c ($\lambda_{em} = 562$ nm: p$K_a = 2.25 \pm 0.04$, at $\lambda_{em} = 605$ nm: p$K_a = 2.17 \pm 0.03$). These results show that the obtained pK_a values are independent of which spectral data are used and of the selected wavelengths. All estimated n values are indicative of a 1 to 1 binding between dye **1** and H^+.

Since large spectral shifts are observed in the fluorescence excitation spectra, the *ratiometric* method (eq 11, see Experimental Section) can be used to estimate values of K_a. The ratio $R = F(\lambda_{em},\lambda_{ex}^1)/F(\lambda_{em},\lambda_{ex}^2)$ of two fluorescence excitation intensities (at $\lambda_{ex}^1 = 600$ nm and $\lambda_{ex}^2 = 553$ nm) with observation at $\lambda_{em} = 660$ nm as a function of pH was used to estimate K_a and n. Figure 13b shows the best fit of eq 11 to the above-defined *ratiometric* fluorescence excitation data, from which values of K_a and n are obtained. The pK_a value from *ratiometric* excitation data estimated on the basis of eq 11 is 2.3 $\pm$ 0.1, in good agreement with that obtained by the *direct* titration method. The estimated n value indicates that **1** binds one proton.

3. Experimental and Theoretical Sections

3.1. Materials. All solvents for the spectroscopic measurements were of spectroscopic grade and were used without further purification. The chemicals for the synthesis were of reagent grade quality, procured from commercial sources and used as received. Boron trifluoride etherate was ca. 48% BF_3.

3.2. NMR and Mass Spectra. ^1H and ^{13}C NMR spectra were recorded on a Bruker Avance 300 instrument operating at a frequency of 300 MHz for ^1H and 75 MHz for ^{13}C. ^1H NMR spectra were referenced to tetramethylsilane (0.00 ppm) as an internal standard and chemical shift multiplicities are reported as s = singlet, d = doublet, and m = multiplet. ^{13}C spectra were referenced to the residual $CDCl_3$ signal (77.67). Low-resolution mass spectra were recorded on a Hewlett-Packard 5989A mass spectrometer in electron impact (EI) mode. High-resolution EI mass spectra were recorded on a Kratos MS50TC system coupled to a Mach 3 processing unit with a resolution of 10000.

3.3. Synthesis of 4. First, 408 mg (3 mmol) of *p*-methoxybenzaldehyde and 570 mg (6 mmol) of 2,4-dimethylpyrrole were dissolved in 50 mL of dry dichloromethane. One drop of trifluoroacetic acid (TFA) was added to the solution and the reaction mixture was stirred for 16 h at room temperature under argon. After disappearance of the aldehyde (monitored via thin-layer chromatography), a solution of 500 mg of *p*-chloranil in dichloromethane (30 mL) was added to the solution and stirring was continued for another 0.5 h. 3 mL of absolute triethylamine was then added to the mixture and after stirring for 15 min, 3 mL of BF_3-OEt_2 was added dropwise. The stirring was continued for the next 2 h and then the mixture was washed with water. The separated organic phase was dried over $MgSO_4$, evaporated, and purified through a silica column (eluent: hexane/ethyl acetate 7/3 v/v) to obtain 402 mg (38%) of shiny red crystals of compound **4**. mp 214−216 °C.

^1H NMR (300 MHz, in $CDCl_3$): 7.20 (d, 2H, $J = 8.2$ Hz, ArH); 7.03 (d, 2H, $J = 9.1$ Hz, ArH); 5.9 (s, 2H, H2 and H6); 3.8 (s, 3H, OCH_3); 2.5 (s, 6H, 2 × CH_3); 1.4 (s, 6H, 2 × CH_3). LRMS: (EI, 70 eV) 354 (M^+ 100), 339 (20), 335 (11), 334 (41). HRMS (EI): calcd for $C_{20}H_{21}BF_2N_2O$, 354.1715; found, 354.1715.

3.4. Synthesis of 1. Compound **4** (70 mg, 0.2 mmol), *p*-*N*,*N*-dimethylaminobenzaldehyde (40 mg, 0.28 mmol), piperidine (0.1 mL), acetic acid (0.1 mL), and a small amount of molecular sieves were suspended in 2 mL of dry toluene in a 10 mL glass tube sealed with a Teflon cap. The sample was irradiated at 200 W and 190 °C for 20 min in a CEM-Discover monomode microwave apparatus. After completion of the reaction, the cold mixture was directly poured into a silica gel column and eluted with a 1/1 (v/v) dichloromethane/hexane mixture. The collected blue fraction was subsequently recrystallized from chloroform/hexane to yield 25 mg (26%) of deep blue crystals of **1**. mp 296−298 °C.

^{1}H NMR (300 MHz, in $CDCl_3$): 7.53 (m, 3H; 2H for ArH; 1H for vinylic); 7.23 (m, 3H; 2H for aromatic (MeOPh); 1H for vinylic); 7.03 (d, 2H, $J = 8.7$, aromatic (MeOPh)); 6.71 (d, 2H, $J = 8.7$, ArH); 6.60 (s, 1H, H6); 5.97 (s, 1H, H2); 3.89 (s, 3H, OCH_3); 3.04 (s, 6H, NMe); 2.59 (s, 3H, CH_3); 1.49 (s, 3H, CH_3); 1.44 (s, 3H, CH_3). ^{13}C NMR (75 MHz, in $CDCl_3$): 14.5, 15.0, 15.3, 40.6, 55.7, 112.4, 114.7, 117.9, 120.7, 125.1, 127.8, 129.6, 130.0, 137.9, 139.3, 141.2, 143.2, 146.0, 151.4, 160.4. LRMS (EI, 70 eV): 486 (19), 485 (M^+100), 484 (11), 450 (9). HRMS (EI): calcd for $C_{29}H_{30}BF_2N_3O$, 485.2450; found, 485.2454.

3.5. Quantum-Chemical Calculations. Ground-state and excited-state geometry optimizations of the isolated molecule in the gas phase have been performed at the AM1/CAS-CI (complete active space−configuration interaction) level.[47,48] These geometries have been subsequently used as input for INDO/S[49]/SCI (single configuration interaction) calculations of the vertical electronic excitations.[50]

The solvent effects have been modeled within a self-consistent reaction field (SCRF) model in the presence of a dielectric continuum. The model assumes that the absorption [emission] process is instantaneous so that only the (fast) electronic polarization of the solvent is allowed to respond to the excited-state [ground-state] charge distribution (i.e., the nuclei are frozen in their initial configuration). In the simplest case of a spherical cavity with radius a, retaining only electrostatic contributions, the solvent shifts for absorption and emission can be expressed as[33]

$$\Delta E_{abs} = E_{ge}^{solvent}(G) - E_{ge}^{gas}(G) = \frac{-2}{4\pi\epsilon_0 a^3}\left\{\bar{\mu}_g(G)\Delta\bar{\mu}_{ge}(G) \times [f(\epsilon) - f(n^2)] + \frac{1}{2}[\bar{\mu}_e^{\,2}(G) - \bar{\mu}_g^{\,2}(G)]f(n^2)\right\} \quad (4)$$

$$\Delta E_{em} = E_{ge}^{solvent}(E) - E_{ge}^{gas}(E) = \frac{-2}{4\pi\epsilon_0 a^3}\left\{\bar{\mu}_e(E)\Delta\bar{\mu}_{ge}(E) \times [f(\epsilon) - f(n^2)] + \frac{1}{2}[\bar{\mu}_e^{\,2}(E) - \bar{\mu}_g^{\,2}(E)]f(n^2)\right\} \quad (5)$$

with

$$f(\epsilon) = \frac{\epsilon - 1}{2\epsilon + 1} \quad \text{and} \quad f(n^2) = \frac{n^2 - 1}{2n^2 + 1} \quad (6)$$

where $\bar{\mu}_g(G)$ denotes the ground-state (subscript "g") dipole in the ground-state geometry (capital "G"); similarly, $\bar{\mu}_e(E)$ is the excited-state dipole in the excited-state geometry; $\Delta\bar{\mu}_{ge}(G) = \bar{\mu}_e(G) - \bar{\mu}_g(G)$ [respectively, $\Delta\bar{\mu}_{ge}(E) = \bar{\mu}_e(E) - \bar{\mu}_g(E)$] corresponds to the dipole moment difference between the ground state and the excited state in the geometry of the ground state [respectively, excited state]. The bar on top of μ indicates the vector nature of the dipole moment. ϵ, n, and a stand for the solvent dielectric constant, the solvent refractive index, and the radius of the spherical cavity in which the fluorophore is contained, respectively. If the same excited state is involved in absorption and emission, i.e., neglecting the influence of geometric relaxation in the excited state: $\bar{\mu}_g(G) = \bar{\mu}_g(E) = \bar{\mu}_g$, $\bar{\mu}_e(E) = \bar{\mu}_e(G) = \bar{\mu}_e$, and $\Delta\bar{\mu}_{ge}(G) = \Delta\bar{\mu}_{ge}(E) = \Delta\bar{\mu}_{ge}$, subtracting eq 4 from eq 5 yields the well-known Lippert−Mataga expression for the Stokes shift:[28,29]

$$\Delta\bar{\nu} = \frac{2\Delta f}{4\pi\epsilon_0 hca^3}(\bar{\mu}_e - \bar{\mu}_g)^2 + \text{constant} \quad (7)$$

$\Delta\bar{\nu} = \bar{\nu}_{abs} - \bar{\nu}_{em}$ is the frequency shift in wavenumbers (cm^{-1}) between absorption ($\bar{\nu}_{abs}$) and fluorescence emission ($\bar{\nu}_{em}$), $\Delta f = f(\epsilon) - f(n^2)$, $h = 6.6262 \times 10^{-34}$ J s is Planck's constant, $c = 2.9979 \times 10^8$ m s^{-1} is the velocity of light, ϵ_0 is the permittivity of vacuum (8.8542×10^{-12} C^2 N^{-1} m^{-2}).

3.6. Steady-State Spectroscopy. The absorption measurements were done on a Perkin-Elmer Lambda 40 UV/vis spectrophotometer. Corrected steady-state excitation and emission spectra were recorded on a SPEX Fluorolog. For the determination of the fluorescence quantum yields (ϕ_f) in solvents 1−18, dilute solutions with an absorbance below 0.1 at $\lambda_{ex} =$ 560 nm were used. Cresyl violet in methanol ($\phi_f = 0.55$) was used as fluorescence standard.[51] For solvent 19, ϕ_f was determined by excitation at 530 nm. The ϕ_f values reported in Table 1 are the averages of multiple (generally 4), fully independent measurements. The ϕ_f values as a function of pH were measured by excitation at 530 nm. In all cases, correction for the refractive index was applied. All spectra were recorded at room temperature on nondegassed samples.

3.7. Time-Resolved Spectroscopy. Fluorescence decay traces of **1** were recorded at several emission wavelengths by the single-photon timing method.[52] Details of the instrumentation used[53] and experimental procedures[54] have been described elsewhere. The samples were excited at 530 or 580 nm with a repetition rate of 8.18 MHz. Fluorescence decay histograms were collected in 4096 channels using 10 × 10 mm cuvettes. The absorbance at the excitation wavelength was always below 0.1. All lifetime measurements were performed on nondegassed samples at 20 °C. Histograms of the instrument response functions (using a LUDOX scatterer) and sample decays were recorded until they typically reached 10^4 counts in the peak channel. The total width at half-maximum of the instrument response function was ~30 ps.

The fitting parameters were determined by nonlinear least-squares estimation by minimizing the global reduced chi-square χ_g^2:

$$\chi_g^{\,2} = \sum_l^q \sum_i w_{li}(y_{li}^{\,o} - y_{li}^{\,c})^2/\nu \quad (8)$$

where the index l sums over q experiments, and the index i sums over the appropriate channel limits for each individual experiment. $y_{li}^{\,o}$ and $y_{li}^{\,c}$ denote respectively the observed and calculated (fitted) values corresponding to the ith channel of the lth experiment, and w_{li} is the corresponding statistical weight. ν represents the number of degrees of freedom for the entire multidimensional fluorescence decay surface.

The statistical criteria to judge the quality of the fit included both graphical and numerical tests and have been described previously.[55] The decays were analyzed first individually by a (multi) exponential decay law in terms of decay times τ_i and their associated preexponential factors α_i. A minimum of three

different observation wavelengths λ_{em} covering the emission spectrum were selected for the construction of the fluorescence decay surface. The final curve-fitting was done by global (or simultaneous) analysis in which decay traces recorded at several λ_{em} were described by a (multi) exponential decay function with linked (global) decay times τ_i and local preexponentials α_i. The goodness-of-fit was judged for each fluorescence decay trace separately as well as for the global fluorescence decay surface. All reported curve fittings had χ^2 values below 1.1.

When the fluorescence decays were monoexponential, the rate constants of radiative (k_f) and nonradiative (k_{nr}) deactivation were calculated from the measured fluorescence quantum yield ϕ_f and lifetime τ according to eq 9:

$$k_f = \phi_f/\tau \tag{9a}$$

$$k_{nr} = (1 - \phi_f)/\tau \tag{9b}$$

3.8. Fluorimetric Titrations. The ground-state acidity constant K_a of the ammonium salt of **1** was determined in acetonitrile solution at 20 °C by *direct* fluorimetric titration as a function of pH using the fluorescence excitation or emission spectra. To adjust the pH of the acetonitrile solutions, 0.1 and 0.01 M solutions of HCl and NaOH in acetonitrile were used. Fitting nonlinear eq 10 (see ref 56 for more information,) to the steady-state fluorescence data F recorded as a function of pH yields values of K_a, the fluorescence signals F_{min} and F_{max} at minimal and maximal [H^+], respectively (corresponding to the amine and ammonium forms of the dye, respectively), and n (the number of protons bound per amine molecule).

$$F = \frac{F_{max}[H^+]^n + F_{min}K_a}{K_a + [H^+]^n} \tag{10}$$

Fitting eq 10 to the steady-state fluorescence data F with n, K_a, F_{min}, and F_{max} as freely adjustable parameters always gave values of n close to 1, indicating that one proton is bound per tertiary amine molecule. Therefore, n was kept fixed at 1 in the final curve fittings, from which the estimated values of K_a are reported here.

Since large spectral shifts are observed in the fluorescence excitation spectra, the *ratiometric* method (eq 11; see ref 56) can be used to estimate values of K_a. In the excitation ratiometric method, one measures $R = F(\lambda_{em},\lambda_{ex}^1)/F(\lambda_{em},\lambda_{ex}^2)$ at a common emission wavelength, λ_{em}, and two different excitation wavelengths, λ_{ex}^1 and λ_{ex}^2. R_{min} and R_{max} correspond to the ratios at *min*imal and *max*imal [H^+], respectively, and $\xi = F_{min}(\lambda_{em},\lambda_{ex}^2)/F_{max}(\lambda_{em},\lambda_{ex}^2)$.

$$R = \frac{R_{max}[H^+]^n + R_{min}K_a\xi}{K_a\xi + [H^+]^n} \tag{11}$$

Fitting nonlinear eq 11 to the excitation ratiometric fluorescence data R as a function of [H^+] yields values for $K_a\xi$, n, R_{min}, and R_{max}. Since $\xi(\lambda_{em},\lambda_{ex}^2)$—the ratio of the fluorescence signal of the amine form of **1** over that of the ammonium form at the indicated excitation and emission wavelengths—is experimentally accessible, a value for K_a can be recovered from ratiometric excitation fluorescence data.

4. Conclusions

We have used a microwave-assisted condensation reaction to synthesize the visible light excitable, fluorescent BODIPY-based dye 3-{2-[4-(dimethylamino)phenyl]ethenyl}-4,4-difluoro-8-(4-methoxyphenyl)-1,5,7-trimethyl-3a,4a-diaza-4-bora-*s*-indacene, which shows strongly solvent dependent fluorescence emission properties. The fluorescence quantum yield and the lifetime decrease in polar solvents in conjunction with large bathochromic shifts. In acetonitrile solution, large spectral shifts are observed in the fluorescence excitation and absorption spectra upon protonation of the tertiary amine function. The value of the acidity constant K_a ($pK_a = 2.25$) of the ammonium form—determined via both *direct* and *ratiometric* fluorimetric titrations—indicates that the dye can be used as a pH indicator in the acidic pH range.

Acknowledgment. Prof. J. Catalán (Universidad Autónoma de Madrid, Spain) is thanked for interesting discussions regarding his set of solvent scales and for the description of the absorption solvatochromism resulting in Figure 9. The authors thank the University Research Fund of the K. U. Leuven for grant GOA 2001/2 and IDO/00/001, and for postdoctoral fellowships to M.B. and W.Q.. The Fonds voor Wetenschappelijk Onderzoek—Vlaanderen (FWO) is acknowledged for grant G.0320.00 N and postdoctoral fellowships to R.A.L.V. and W.M.D.B.. D.B. is a research associate of the FNRS. The joint K. U. Leuven-U. MH. work has been partly supported by the Belgian Federal Science Policy through the IAP—V-03 program. C.F. is supported by the IAP-V-03 program. Ms. Alina Stefan is thanked for technical help with the single-photon timing measurements. The IWT is acknowledged for Grant ZWAP04/007.

References and Notes

(1) Desvergne, J.-P., Czarnik, A. W., Eds. *Chemosensors of Ion and Molecule Recognition*; Kluwer: Dordrecht, The Netherlands, 1997.

(2) Haugland, R. P. *The Handbook. A Guide to Fluorescent Probes and Labeling Technologies*, 10th ed.; Molecular Probes, Inc.: Eugene, OR, 2005.

(3) Treibs, A.; Kreuzer, F.-H. *Liebigs Ann. Chem.* **1968**, *718*, 208−223.

(4) Valeur, B. *Molecular Fluorescence. Principles and Applications.* Wiley-VCH: Weinheim, 2002.

(5) (a) Baruah, M.; Qin, W.; Basarić, N.; De Borggraeve, W. M.; Boens, N. *J. Org. Chem.* **2005**, *70*, 4152−4157. (b) Qin, W.; Baruah, M.; Stefan, A.; Van der Auweraer, M.; Boens, N. *ChemPhysChem* **2005**, *6*, 2343−2351.

(6) Yamada, K.; Nomura, Y.; Citterio, D.; Iwasawa, N.; Suzuki, K. *J. Am. Chem. Soc.* **2005**, *127*, 6956−6957.

(7) (a) Malval, J.-P.; Leray, I.; Valeur, B. *New J. Chem.* **2005**, *29*, 1089−1094. (b) Baruah, M.; Qin, W.; Vallée, R. A. L.; Beljonne, D.; Rohand, T.; Dehaen, W.; Boens, N. *Org. Lett.* **2005**, *7*, 4377−4380.

(8) Basarić, N.; Baruah, M.; Qin, W.; Metten, B.; Smet, M.; Dehaen, W.; Boens, N. *Org. Biomol. Chem.* **2005**, *3*, 2755−2761.

(9) Coskun, A.; Akkaya, E. U. *J. Am. Chem. Soc.* **2005**, *127*, 10464−10465.

(10) Wu, Y.; Peng, X.; Guo, B.; Fan, J.; Zhang, Z.; Wang, J.; Cui, A.; Gao, Y. *Org. Biomol. Chem.* **2005**, *3* 1387−1392.

(11) Seo, T. S.; Bai, X.; Kim, D. H.; Meng, Q.; Shi, S.; Ruparel, H.; Li, Z.; Turro, N. J.; Ju, J. *Proc. Natl. Acad. Sci. U.S.A.* **2005**, *102*, 5926−5931.

(12) Yee, M.-c.; Fas, S. C.; Stohlmeyer, M. M.; Wandless, T. J.; Cimprich, K. A. *J. Biol. Chem.* **2005**, *280*, 29053−29059.

(13) Vos de Wael, E.; Pardoen, J. A.; van Koeveringe, J. A.; Lugtenburg, J. *Trav. Chim. Pays-Bas* **1977**, *96*, 306−309.

(14) Karolin, J.; Johansson, L. B.-Å.; Strandberg, L.; Ny, T. *J. Am. Chem. Soc.* **1994**, *116*, 7801−7806.

(15) Bergström, F.; Mikhalyov, I.; Hägglöf, P.; Wortmann, R.; Ny, T.; Johansson, L. B.-Å. *J. Am. Chem. Soc.* **2002**, *124*, 196−204.

(16) Rurack, K.; Kollmannsberger, M.; Resch-Genger, U.; Daub, J. *J. Am. Chem. Soc.* **2000**, *122*, 968−969.

(17) Rurack, K.; Kollmannsberger, M.; Daub, J. *Angew. Chem., Int. Ed.* **2001**, *40*, 385−387.

(18) Costela, A.; García-Moreno, I.; Gomez, C.; Sastre, R.; Amat-Guerri, F.; Liras, M.; López Arbeloa, F.; Bañuelos Prieto, J.; López Arbeloa, I. *J. Phys. Chem. A* **2002**, *106*, 7736−7742.

(19) Kollmannsberger, M.; Rurack, K.; Resch-Genger, U.; Daub, J. *J. Phys. Chem. A* **1998**, *102*, 10211−10220.

(20) López Arbeloa, T.; López Arbeloa, F.; López Arbeloa, I.; García-Moreno, I.; Costela, A.; Sastre, R.; Amat-Guerri, F. *Chem. Phys. Lett.* **1999**, *299*, 315−321.

(21) López Arbeloa, F.; Bañuelos Prieto, J.; Martínez Martínez, V.; Arbeloa López, T.; López Arbeloa, I. *ChemPhysChem* **2004**, *5*, 1762−1771.

(22) Bañuelos Prieto, J.; López Arbeloa, F.; Martínez Martínez, V.; Arbeloa López, T.; Amat-Guerri, F.; Liras, M.; López Arbeloa, I. *Chem. Phys. Lett.* **2004**, *385*, 29−35.

(23) Qin, W.; Baruah, M.; Van der Auweraer, M.; De Schryver, F. C.; Boens, N. *J. Phys. Chem. A* **2005**, 109, 7371−7384.

(24) Moon, S. Y.; Cha, N. R.; Kim, Y. H.; Chang, S.-K. *J. Org. Chem.* **2004**, *69*, 181−183.

(25) Fukuzumi, S.; Yoshida, Y.; Okamoto, K.; Imahori, H.; Araki, Y.; Ito, O. *J. Am. Chem. Soc.* **2002**, *124*, 6794−6795.

(26) Palit, D. K.; Zhang, T.; Kumazaki, S.; Yoshihara, K. *J. Phys. Chem. A* **2003**, *107*, 10798−10804.

(27) van der Meer, M. J.; Zhang, H.; Rettig, W.; Glasbeek, M. *Chem. Phys. Lett.* **2000**, 320, 673−680.

(28) Lippert, E. *Z. Naturforsch., A: Phys. Sci.* **1955**, *10*, 541−545.

(29) Mataga, N.; Kaifu, Y.; Koizumi, M. *Bull. Chem. Soc. Jpn.* **1955,** *28*, 690−691 and **1956**, *29*, 465−470.

(30) Karelson, M. M.; Zerner, M. C. *J. Phys. Chem.* **1992**, *96*, 6949−6957.

(31) Convergence problems are encountered in polar solvents for $a =$ 4.8 Å.

(32) Kawski, A. *Z. Naturforsch. A* **2002**, *57a*, 255−262.

(33) (a) Tomasi, J.; Persico, M. *Chem. Rev.* **1994**, *94*, 2027−2094. (b) McRae, E. G. *J. Phys. Chem.* **1957**, *61*, 562−572.

(34) Reichardt, C. *Chem. Rev.* **1994**, *94*, 2319−2358.

(35) Kamlet, M. J.; Taft, R. W. *J. Am. Chem. Soc.* **1976**, *98*, 377−383.

(36) Catalán, J. *J. Org. Chem.* **1997**, *62*, 8231−8234.

(37) *Handbook of solvents*; Wypych, G., Ed.; ChemTec Publishing: Toronto, Canada, 2001; pp 583−616.

(38) Catalán, J.; Palomar, J.; Díaz, C.; de Paz, J. L. G. *J. Phys. Chem. A* **1997**, *101*, 5183−1589.

(39) Marcus, Y. *Chem. Soc. Rev.* **1993**, *22*, 409−416.

(40) Catalán, J.; Hopf, H. *Eur. J. Org. Chem.* **2004**, 4694−4702.

(41) Birks, J. B. *Photophysics of Aromatic Molecules*; Wiley-Interscience: London, 1970.

(42) (a) Verbeek, G.; Depaemelaere, S.; Van der Auweraer, M.; De Schryver, F. C.; Vaes, A.; Terrell, D.; De Meutter, S. *Chem. Phys.* **1993**, *176*, 195−213. (b) Verbouwe, W.; Van der Auweraer, M.; De Schryver, F. C.; Masuhara, H.; Pansu, R.; Faure, J. *J. Phys. Chem. A* **1997**, *101*, 8157−8165.

(43) Van der Auweraer, M.; Viaene, L.; Van Haver, Ph.; De Schryver, F. C. *J. Phys. Chem.* **1993**, *97*, 7178−7184.

(44) (a) Siders, P.; Marcus, R. A. *J. Am. Chem. Soc.* **1981**, *103*, 741−747. (b) Marcus, R. A. *J. Chem. Phys.* **1984**, *81*, 4494−4500. (c) Jortner, J.; Bixon, M. *J. Chem. Phys.* **1988**, *88*, 167−170.

(45) Tominaga, K.; Walker, G. C.; Kang, T. J.; Barbara, P. F.; Fonseca, T. *J. Phys. Chem.* **1991**, *95*, 10485−10492.

(46) This is the "gap law".

(47) (a) Dewar, M. J. S.; Zoebisch, E. G.; Healy, E. F.; Stewart, J. J. P. *J. Am. Chem. Soc.* **1985**, *107*, 3902−3909. (b) AMPAC 8. Semichem, Inc. PO Box 1649, Shawnee, KS 66222, 1992−2004.

(48) The active space comprises the eight most frontier molecular orbitals.

(49) Ridley, J.; Zerner, M. *Theor. Chim. Acta* **1973**, *32*, 111−134.

(50) The active space includes the 60 highest occupied molecular orbitals (MOs) and 60 lowest unoccupied MOs.

(51) Olmsted, J. *J. Phys. Chem.* **1979**, *83*, 2581−2584.

(52) (a) O'Connor, D. V.; Phillips, D. *Time-correlated Single Photon Counting*; Academic Press: New York, 1984. (b) Boens, N. In *Luminescence Techniques in Chemical and Biochemical Analysis*; Baeyens, W. R. G., De Keukeleire, D., Korkidis, K., Eds.; Marcel Dekker: New York, 1991; pp 21−45.

(53) Maus, M.; Rousseau, E.; Cotlet, M.; Schweitzer, G.; Hofkens, J.; Van der Auweraer, M.; De Schryver, F. C.; Krueger, A. *Rev. Sci. Instrum.* **2001**, *72*, 36−40.

(54) Crovetto, L.; Orte, A.; Talavera, E. M.; Alvarez-Pez, J. M.; Cotlet, M.; Thielemans, J.; De Schryver, F. C.; Boens, N. *J. Phys. Chem. B*, **2004**, *108*, 6082−6092.

(55) Van den Zegel, M.; Boens, N.; Daems, D.; De Schryver, F. C. *Chem. Phys.* **1986**, *101*, 311−335.

(56) Cielen, E.; Stobiecka, A.; Tahri, A.; Hoornaert, G. J.; De Schryver, F. C.; Gallay, J.; Vincent, M.; Boens, N. *J. Chem. Soc., Perkin Trans. 2* **2002**, 1197−1206.